



# Two-dimensional Hybrid Simulations of Filamentary Structures and Kinetic Slow Waves Downstream of a Quasi-parallel Shock

Yufei Hao<sup>1,2,3</sup>, Quanming Lu<sup>1,3</sup>, Xinliang Gao<sup>1,3</sup>, Huanyu Wang<sup>1,3</sup>, Dejin Wu<sup>4</sup>, and Shui Wang<sup>1,3</sup><sup>1</sup> CAS Key Laboratory of Geospace Environment, Department of Geophysics and Planetary Science, University of Science and Technology of China, Hefei 230026, People's Republic of China; [qmlu@ustc.edu.cn](mailto:qmlu@ustc.edu.cn)<sup>2</sup> State Key Laboratory of Space Weather, Chinese Academy of Sciences, Beijing 100190, People's Republic of China<sup>3</sup> Collaborative Innovation Center of Astronautical Science and Technology, People's Republic of China<sup>4</sup> Purple Mountain Observatory, Chinese Academy of Sciences, Nanjing 210008, People's Republic of China

Received 2018 January 31; revised 2018 May 27; accepted 2018 June 5; published 2018 July 3

## Abstract

In this paper, with two-dimensional hybrid simulations, we study the generation mechanism of filamentary structures downstream of a quasi-parallel shock. The results show that in the downstream both the amplitude of magnetic field and number density exhibit obvious filamentary structures, and the magnetic field and number density are anticorrelated. Detailed analyses find that these downstream compressive waves propagate almost perpendicular to the magnetic field, and the dominant wave number is around the inverse of the ion kinetic scale. Their parallel and perpendicular components roughly satisfy  $\delta B_{\parallel}/\delta B_{\perp} = \sqrt{1 + 1/\rho_i^2 k_{\perp}^2}$  (where  $\delta B_{\parallel}$  and  $\delta B_{\perp}$  represent the parallel and in-plane perpendicular components of magnetic field,  $k_{\perp}$  is the wave number in the perpendicular direction, and  $\rho_i$  in the ion gyroradius), and their Alfvén ratio also roughly agrees with the analytical relation  $R_{Ai} = (1 + 2\rho_i^2 k_{\perp}^2)/\beta$  (where  $R_{Ai}$  and  $\beta$  indicate the Alfvén ratio and plasma beta, respectively), while the corresponding cross helicity and compressibility show good agreement with previous theoretical calculations. All of these properties are consistent with those of kinetic slow waves (KSWs). Therefore, we conclude that the filamentary structures downstream of a quasi-parallel shock are produced by the excitation of KSWs.

*Key words:* methods: numerical – plasmas – shock waves – waves

## 1. Introduction

Collisionless shocks are universal and thought to be responsible for the almost power-law spectra of energetic particles in space and astrophysical plasma (Jones & Ellison 1991; Zank et al. 2000, 2001; Giacalone & Decker 2010). Around a shock, the incident flow energy can be efficiently converted into the thermal energy and lead to the possible generation of energetic particles. The accelerated particles always result in a non-equilibrium state of ion velocity distribution that may lead to the generation of various waves around the shock front in most instances (Krauss-Varban & Omid 1991; Scholer et al. 1993; Krauss-Varban 1995; Yang et al. 2009a, 2009b; Su et al. 2012a, 2012b; Ofman & Gedalin 2013; Wilson et al. 2013; Hao et al. 2014, 2016a, 2016b; Tsubouchi et al. 2016). Especially at quasi-parallel shocks, where the upstream background magnetic field is approximately parallel to the shock normal, the accelerated particles can easily leak to the upstream (Omid et al. 2013, 2016), and waves will be driven in the shock front and upstream due to the interaction of these particles with incident flow (Krauss-Varban & Omid 1991; Scholer et al. 1993; Krauss-Varban 1995; Guo & Giacalone 2013).

Downstream waves at quasi-parallel shocks have thoroughly been investigated with hybrid simulations (Krauss-Varban & Omid 1991; Scholer et al. 1993; Krauss-Varban 1995; Scholer et al. 1997). It is believed that the waves excited in the shock front and upstream region play an important role in the evolution of downstream fluctuations (Krauss-Varban & Omid 1991; Scholer et al. 1993). In more parallel shocks ( $\theta_{Bn} \sim 10^\circ$ , where  $\theta_{Bn}$  is defined as the angle between the upstream background magnetic field and the shock normal), the particles from the upstream and downstream populations can overlap in the shock front and form unstable beams that will

drive the interface instability (Krauss-Varban 1995; Scholer et al. 1997). This instability can excite the downstream interface waves, and they will be quickly damped over a short distance from the shock front (Krauss-Varban 1995). Instead, in the case of more oblique shocks ( $\theta_{Bn} \sim 30^\circ$ ), downstream waves can be mostly attributed to the mode conversion of upstream ultra-low-frequency (ULF) waves, which are essentially fast magnetosonic waves excited by the interaction of reflected particles with the incident flow. With one-dimensional (1D) hybrid simulations, Krauss-Varban & Omid (1991) found that the upstream ULF waves can be brought back into the shock front and mode converted into Alfvén/ion cyclotron waves, and they speculated that slow waves can also be generated simultaneously in this process. However, in their 1D hybrid simulations, the propagation direction of the slow waves is assumed to be along the shock normal direction. In this paper, we used a two-dimensional (2D) hybrid simulation model to investigate the detailed properties of slow waves in the downstream of a supercritical quasi-parallel shock, and the formation of the filamentary structures.

## 2. Simulation Model

In our hybrid simulation model, the incident flow has a fixed bulk velocity along the  $x$  direction pointing to the right boundary, which is a rigid boundary and will reflect the injected particles. Then, the reflected particles interact with the injected flow, and the interaction results in the generation of a shock front that moves to the left with a velocity  $V_{sh} \sim 1V_A$  (where  $V_A$  is the upstream Alfvén speed). The fixed bulk velocity of the injected flow is  $4.5V_A$ , so the resulting Mach number of the shock front is about 5.5. The background magnetic field lies in the  $x$ - $y$  simulation plane and is slightly

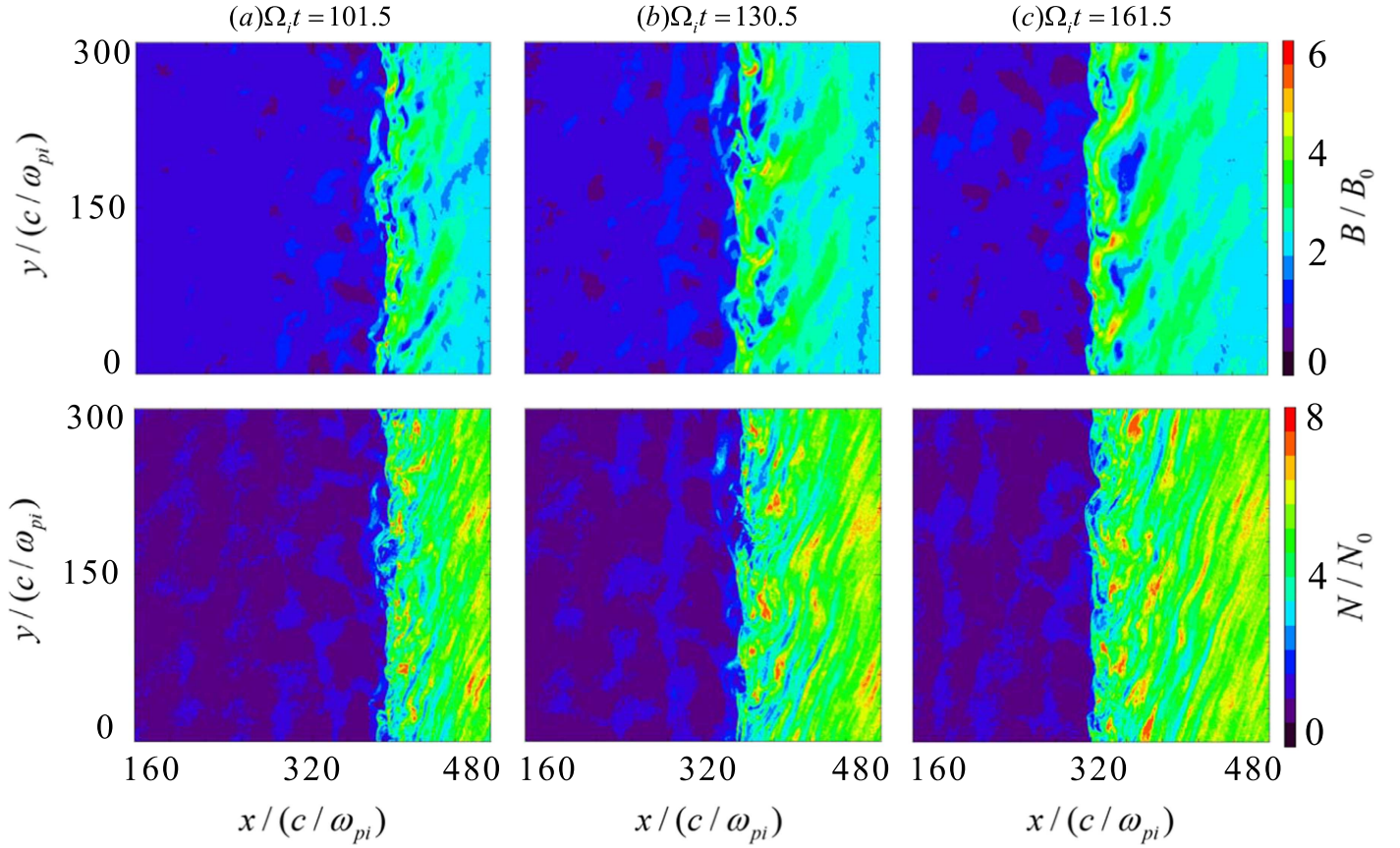


**Figure 1.** The total magnetic fields and particle number density in the  $x$ - $y$  simulation plane at times  $\Omega_i t =$  (a) 101.5, (b) 131.5, and (c) 161.5.

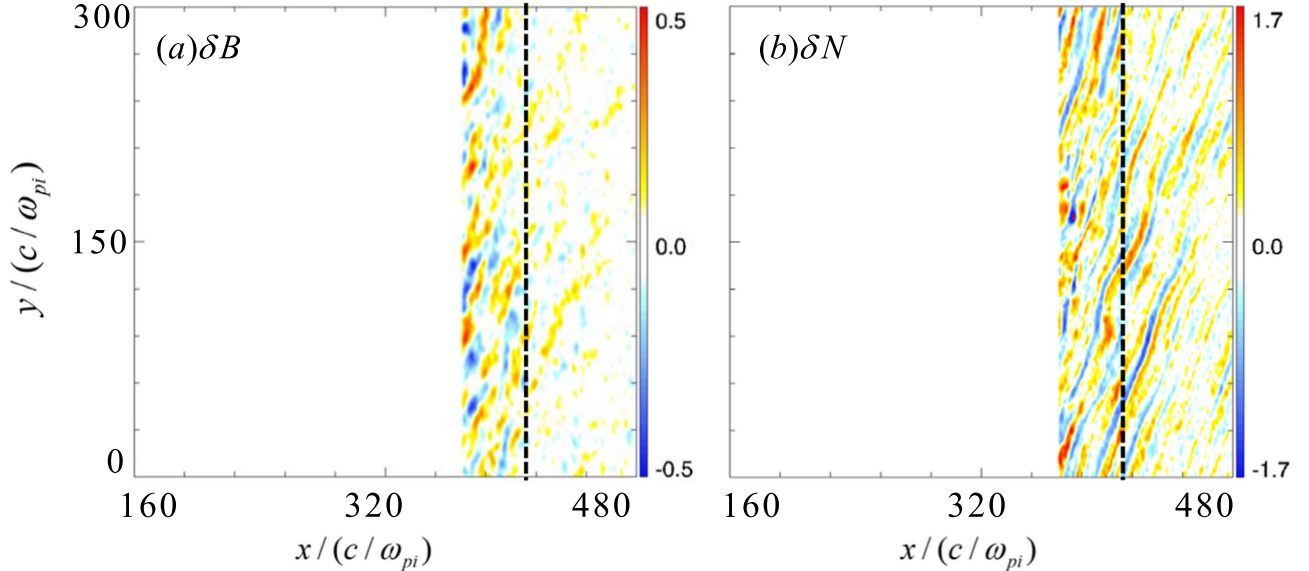


**Figure 2.** The variations of (a) total magnetic field and (b) particle number density, in which the black dashed lines are located at  $x = 375c/\omega_{pi}$ . The contour plots cover an area  $(370c/\omega_{pi} < x < 480c/\omega_{pi}, 0c/\omega_{pi} < y < 300c/\omega_{pi})$ .

oblique to the  $-x$  direction or the shock normal with an angle  $\theta_{Bn} = 30^\circ$ . The upstream beta is set to be  $\beta_p = \beta_e = 0.4$  (where p and e indicate the protons and electrons, respectively), and the electron resistivity length is  $L_\eta = \eta c^2 / (4\pi V_A) = 0.1$ , where  $c$  and  $\eta$  indicate the light speed and the interaction of particles with the high-frequency waves. Here, the grid cell is  $n_x \times n_y = 1000 \times 300$  and grid sizes are  $\Delta x = 0.5c/\omega_{pi}$  and  $\Delta y = 1.0c/\omega_{pi}$  (where  $\omega_{pi}$  denotes the ion plasma frequency).

The time step is  $\Omega_i t = 0.02$  (where  $\Omega_i$  is the ion gyro-frequency).

### 3. Simulation Results

Figure 1 illustrates the total magnetic field and particle number density in the simulation plane at times  $\Omega_i t =$  (a) 101.5, (b) 131.5, and (c) 161.5. In the upper panels, where the

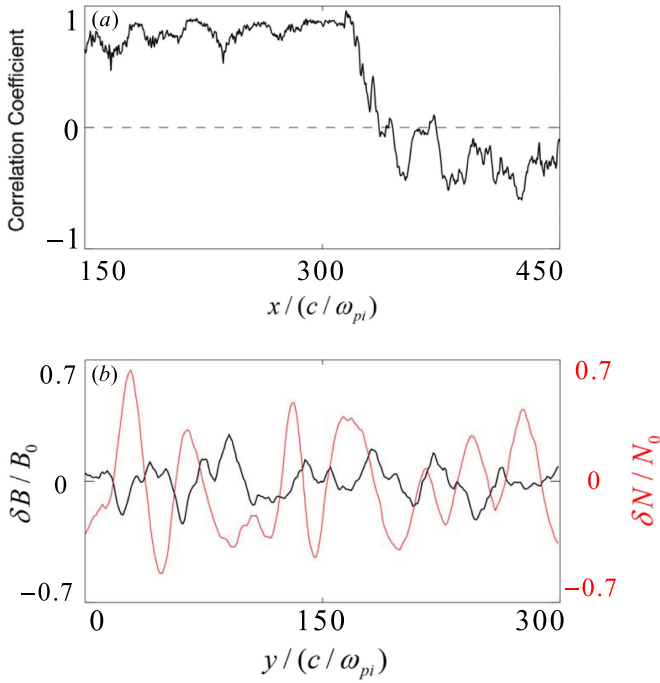


**Figure 3.** (a) The correlation coefficient between magnetic field and particle number density at time  $\Omega_i t = 161.5$  and (b) corresponding values along the black dashed lines in Figure 2.

total magnetic fields are plotted, we can clearly see rippled shock fronts at the three times. Meanwhile, prior to the shock fronts, waves permeate the upstream regions (Scholer et al. 1993; Hao et al. 2016a). The shocked regions are also turbulent areas where we can at least see several large-scale filamentary magnetic structures extending further downstream (Hao et al. 2017). However, in the lower panels, where we present the particle number density, smaller-scale number density fluctuations are observable in the downstream (Omidi et al. 2014) as well as variations of number density in upstream regions due to the compressive ULF waves (Eastwood et al. 2002). Note that the downstream number density fluctuations are not consistent with those large-scale downstream magnetic structures intuitively, although all their structures extend far downstream and nearly lie in the same direction.

For a detailed analysis of their relation, in Figure 2 we plot the magnetic field perturbation  $\delta B = B_t - \bar{B}_t$  and particle number density perturbation  $\delta N = N_i - \bar{N}_i$  in an area ( $370c/\omega_{pi} < x < 480c/\omega_{pi}$ ,  $< y < 300c/\omega_{pi}$ ) at time  $\Omega_i t = 161.5$ , where  $B_t$  is the total magnetic field,  $N_i$  is the particle number density,  $\bar{B}_t$  is the local spatially averaged magnetic field, and  $\bar{N}_i$  is the local spatially averaged number density. Then, we can see the distinct smaller-scale filamentary structures in both of Figures 2(a) and (b), and they all extend further downstream and are nearly parallel to the direction of downstream background magnetic field. More importantly, the scales of magnetic field perturbation and number density perturbation seem to be comparable in the whole selected downstream area. This implies that in the downstream, smaller-scale magnetic structures corresponding to the filamentary structures of downstream number density are embedded in the large-scale magnetic structures, so that we cannot identify these smaller-scale structures of total magnetic fields in Figure 1. In Figure 3, we show their correlation coefficient and the corresponding values along the black dashed lines in Figure 2. The

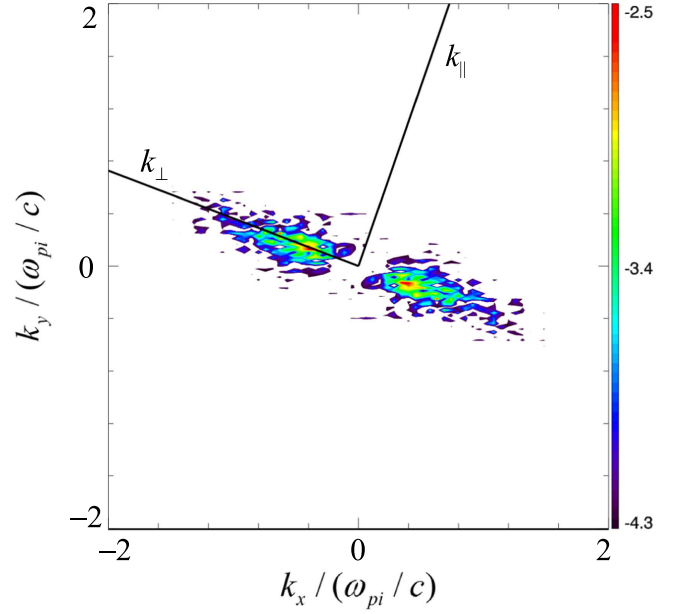


**Figure 4.** Power spectrum of the number density shown in Figure 2(b). The black solid lines denote the  $k_{\parallel} - k_{\perp}$  frame.

correlation coefficient is defined as

$$CC_{Bn}(n_{x0}) = \frac{\sum_{i=nx0, j=1}^{i=nx0, j=ny} ((B_t - \bar{B}_t)(N_i - \bar{N}_i))}{\sqrt{\sum_{i=nx0, j=1}^{i=nx0, j=ny} (B_t - \bar{B}_t)^2 \sum_{i=nx0, j=1}^{i=nx0, j=ny} (N_i - \bar{N}_i)^2}}$$

where  $B_t$  is the total magnetic field for one specific grid point,  $\bar{B}_t$  is the mean magnetic field along the  $y$  direction,  $N_i$  is the corresponding number density of particles,  $\bar{N}_i$  is the mean number density of particles along the  $y$  direction, and  $n_{x0}$  is a specific grid point in the  $x$  direction. It can quantitatively present the relation between the magnetic field and number density in the upper panel where, in the upstream region, it is close to one but below zero looking at the nearly all of the downstream. This scenario implies that in the upstream, magnetic fields are positively correlated with the particle number density while they are anticorrelated in the downstream. In the lower panel, the corresponding values along the red dashed lines in Figure 2 also represent their downstream anticorrelation. In general, the upstream ULF waves are considered to be fast magnetosonic waves, and they can always be observed in the foreshock region before the quasi-parallel shock around the Earth (Eastwood et al. 2004, 2005a, 2005b) and the Venus (Shan et al. 2014, 2016). Therefore, the upstream correlation between magnetic field and number density is reasonable, but the reason for their anticorrelation in the downstream is unclear. One possibility is that there may be some corresponding compressive wave modes, including the possible slow waves proposed by Krauss-Varban & Omidi (1991), and they should have the anticorrelated fluctuations in magnetic field and number density.

To further investigate these fluctuations in the downstream, in Figure 4 we display the power spectrum ( $k_x, k_y$ ) of the fluctuating number density as shown in Figure 2(b). The black solid lines denote the  $k_{\parallel}$  and  $k_{\perp}$ . As illustrated in the wave spectrum, the possible wave modes are highly oblique or nearly perpendicular to the background magnetic field, which is quite

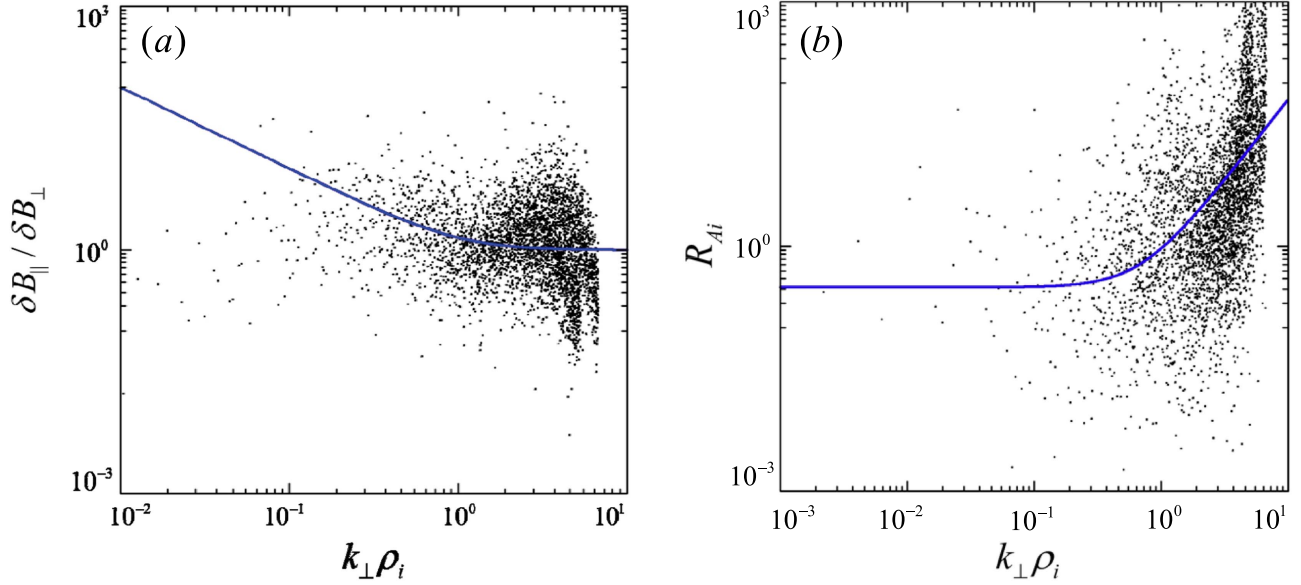


**Figure 5.** The black dots indicate the wave spectrum of magnetic polarization  $\delta B_{\parallel}(k_{\perp})/\delta B_{\perp}(k_{\perp})$  and Alfvén ratio as a function of  $k_{\perp} \rho_i$  in the area shown in Figure 2(a), and their corresponding analytical relations  $\delta B_{\parallel}/\delta B_{\perp} = \sqrt{1 + 1/\rho_i^2 k_{\perp}^2}$  and  $R_{Ai} = (1 + 2\rho^2 k_{\perp}^2)/\beta$  are denoted as the blue lines.

different from the description in Krauss-Varban & Omid (1991). An analysis indicates that the scales of these possible wave modes are mainly around a kinetic scale. This means that if the number density fluctuations result from some wave modes, their wave vectors in the direction perpendicular to the background magnetic field are comparable to the gyroradius of particles, namely,  $\rho_i k_{\perp}$  mainly varies around one. Under the kinetic scale condition, two types of wave modes are widely discussed and studied: kinetic Alfvén waves (KAWs) and kinetic slow waves (KSWs). These two types of wave modes are very similar to each other: both of them can lead to parallel currents, parallel electric fields, and compressive component of fluctuations, which can all accelerate particles in the direction parallel and perpendicular to the background magnetic field under some certain conditions (Narita & Marsch 2015). But, recently, Zhao et al. (2014) provide a way to identify these two types of wave modes by their theoretical properties derived from an isotropic two-fluid plasma model. Therefore, we can use the opposite properties between them to address the questions of whether there are kinetic wave modes and which wave modes they are.

In Figure 5, with the properties described by Zhao et al. (2014) to differential KAWs and KSWs, we plot the ratio of magnetic fluctuations in the direction parallel and perpendicular to the background magnetic field and the Alfvén ratio in the area  $(370c/\omega_{pi} \leq x \leq 480c/\omega_{pi}, 0c/\omega_{pi} \leq y \leq 300c/\omega_{pi})$  as shown in Figure 2(a). The black dots in Figure 5 indicate the dependence of  $\delta B_{\parallel}(k_{\perp})/\delta B_{\perp}(k_{\perp})$  and  $R_{Ai} = \delta v_i(k_{\perp})^2/\delta v_B(k_{\perp})^2$  on  $k_{\perp}$  obtained from the selected area, where  $\delta B_{\parallel}(k_{\perp})$ ,  $\delta B_{\perp}(k_{\perp})$ ,  $\delta v_i(k_{\perp})$  and  $\delta v_B(k_{\perp})$  are the Fourier spectra of parallel component  $\delta B_{\parallel}$ , in-plane perpendicular component  $\delta B_{\perp}$ , particle velocity perturbation  $\delta v_i$  and magnetic perturbation  $\delta v_B$  in units of Alfvén speed. The blue lines denote the theoretical relations  $\delta B_{\parallel}/\delta B_{\perp} = \sqrt{1 + 1/\rho_i^2 k_{\perp}^2}$  and  $R_{Ai} = (1 + 2\rho^2 k_{\perp}^2)/\beta$  of KSWs. We can see that the distribution trend of these black dots is roughly consistent to the theoretical relations from the large scale to small scale, and most of the dots are distributed

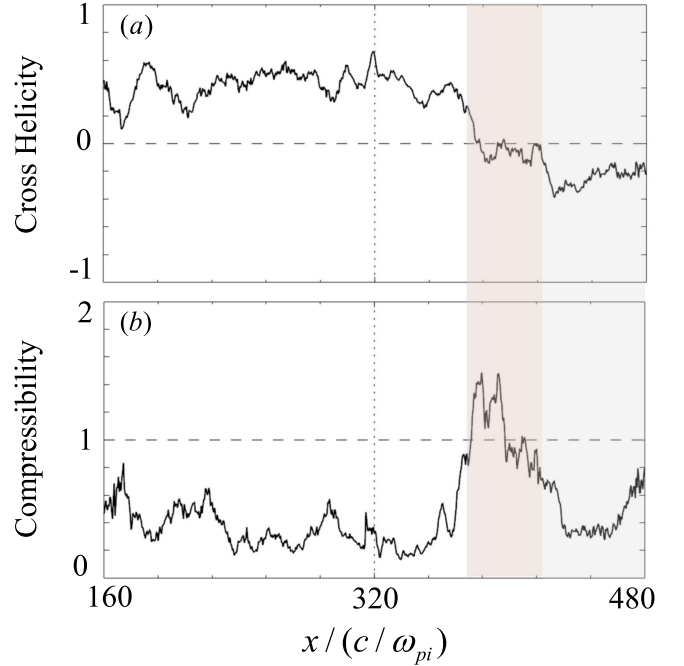


**Figure 6.** The spatial variation of (a) the cross helicity, and (b) the compressibility along the  $x$  direction at time  $\Omega_i t = 161.5$  are shown in Figure 6, where the vertical dotted lines at  $x = 320c/\omega_{pi}$  denote the shock front.

around the kinetic scale. Therefore, we speculate that the downstream filamentary structures of particle number density are attributed to some kinetic wave modes that are KSWs.

To provide more evidence, the corresponding spatial variation the cross helicity and compressibility along the  $x$  direction at time  $\Omega_i t = 161.5$  are shown in Figure 6, where the vertical dotted lines at  $x = 320c/\omega_{pi}$  indicate the shock front. The cross helicity is defined as (Gary & Winske 1992; Yao et al. 2013)

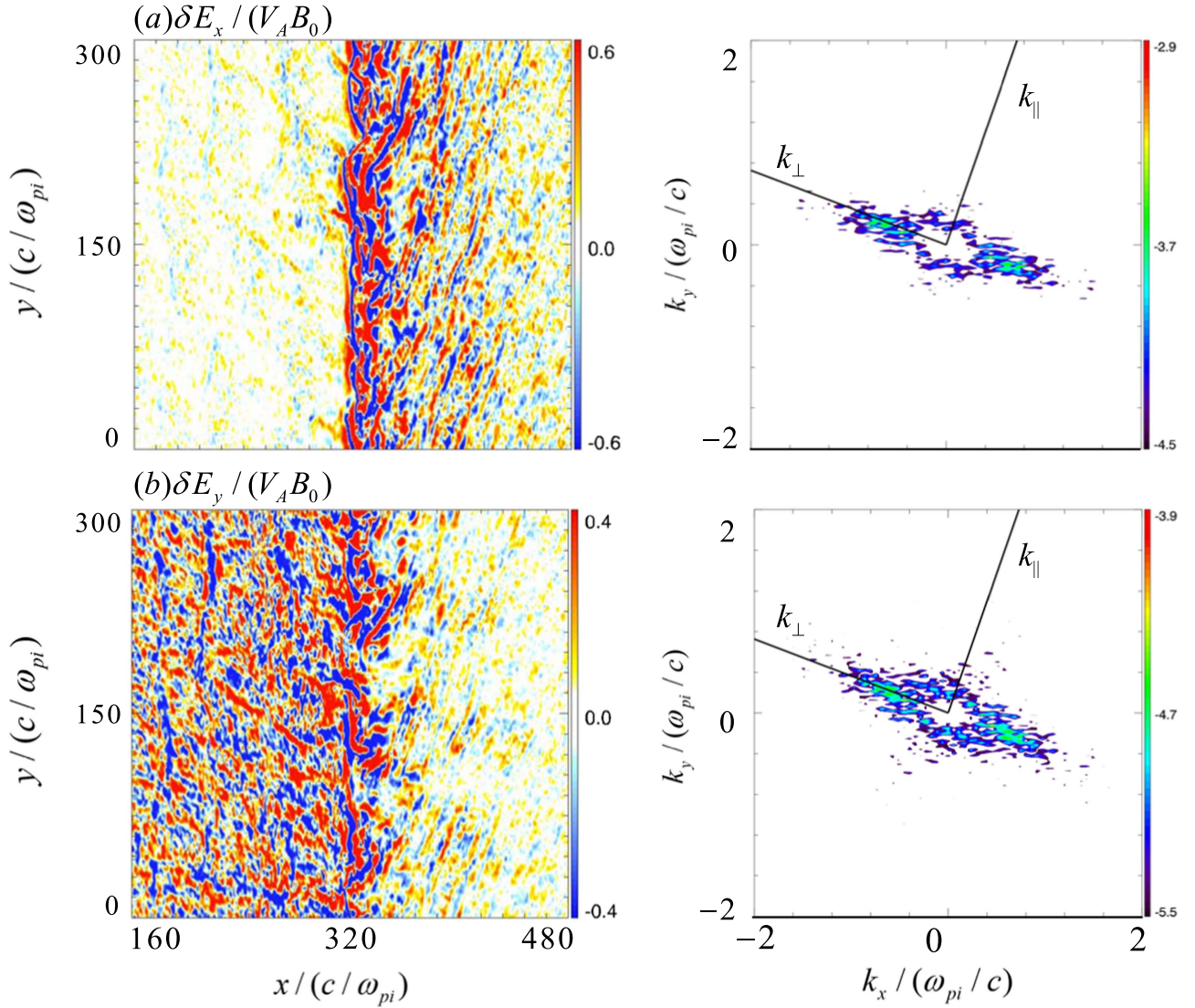


**Figure 7.** Electric fluctuations in the simulation plane and the corresponding power spectrum in the area  $(370c/\omega_{pi} < x < 480c/\omega_{pi}, 0c/\omega_{pi} < y < 300c/\omega_{pi})$  at time  $\Omega_i t = 161.5$ . The black solid lines denote the  $k_{\parallel} - k_{\perp}$  frame.

$$\sigma_c(n_{x0}) = \frac{2\sqrt{N_i} \cdot \sum_{i=nx0, j=1}^{i=nx0, j=ny} ((V_i - \bar{V}_i) \cdot (B - \bar{B}))}{N_i \cdot \sum_{i=nx0, j=1}^{i=nx0, j=ny} ((V_i - \bar{V}_i) \cdot (V_i - \bar{V}_i)) + \sum_{i=nx0, j=1}^{i=nx0, j=ny} ((B - \bar{B}) \cdot (B - \bar{B}))}$$

where  $V_i$  is the average velocity of particles around one specific grid point,  $\bar{V}_i$  is the average value along  $y$  direction,  $B$  is the magnetic field, and  $\bar{B}$  is the mean magnetic field along the  $y$  direction. The compressibility is defined as (Gary 1986)

$$C_p(n_{x0}) = \frac{(B_i - \bar{B}_i)^2 \cdot \sum_{i=nx0, j=1}^{i=nx0, j=ny} (N_i - \bar{N}_i)^2}{\bar{N}_i^2 \cdot \sum_{i=nx0, j=1}^{i=nx0, j=ny} ((B - \bar{B}) \cdot (B - \bar{B}))}$$

In Figure 6, behind the shock front, we can see that the cross helicity in the region marked by a pink shaded stripe is around zero or smaller than zero, and the compressibility exceeds one. This is consistent with the theoretical results described in Table 1(b) of oblique slow waves by Gary & Winske (1992), and both of the two quantities are very similar to the case of oblique slow waves observed by WIND in the quiet solar wind

at 1 au (Yao et al. 2013). Additionally, in the region marked by a gray shaded stripe further away from the shock front, the cross helicity and compressibility become smaller, which is in agreement with the corresponding theoretical values of KSWs (Zhao et al. 2014). Therefore, we can imagine that oblique slow waves may be generated in the immediate downstream by the mode conversion of upstream ULF waves, and then these waves may be strongly dissipated while highly oblique wave modes can last until further downstream due to their lower damping rate (Narita & Marsch 2015).

In Figure 7, we also plot the  $x$  and  $y$  components of electric fields and their corresponding wave spectra in the same area as in Figure 4. It can be seen that the upstream and downstream electric fields all show strong fluctuations, among which

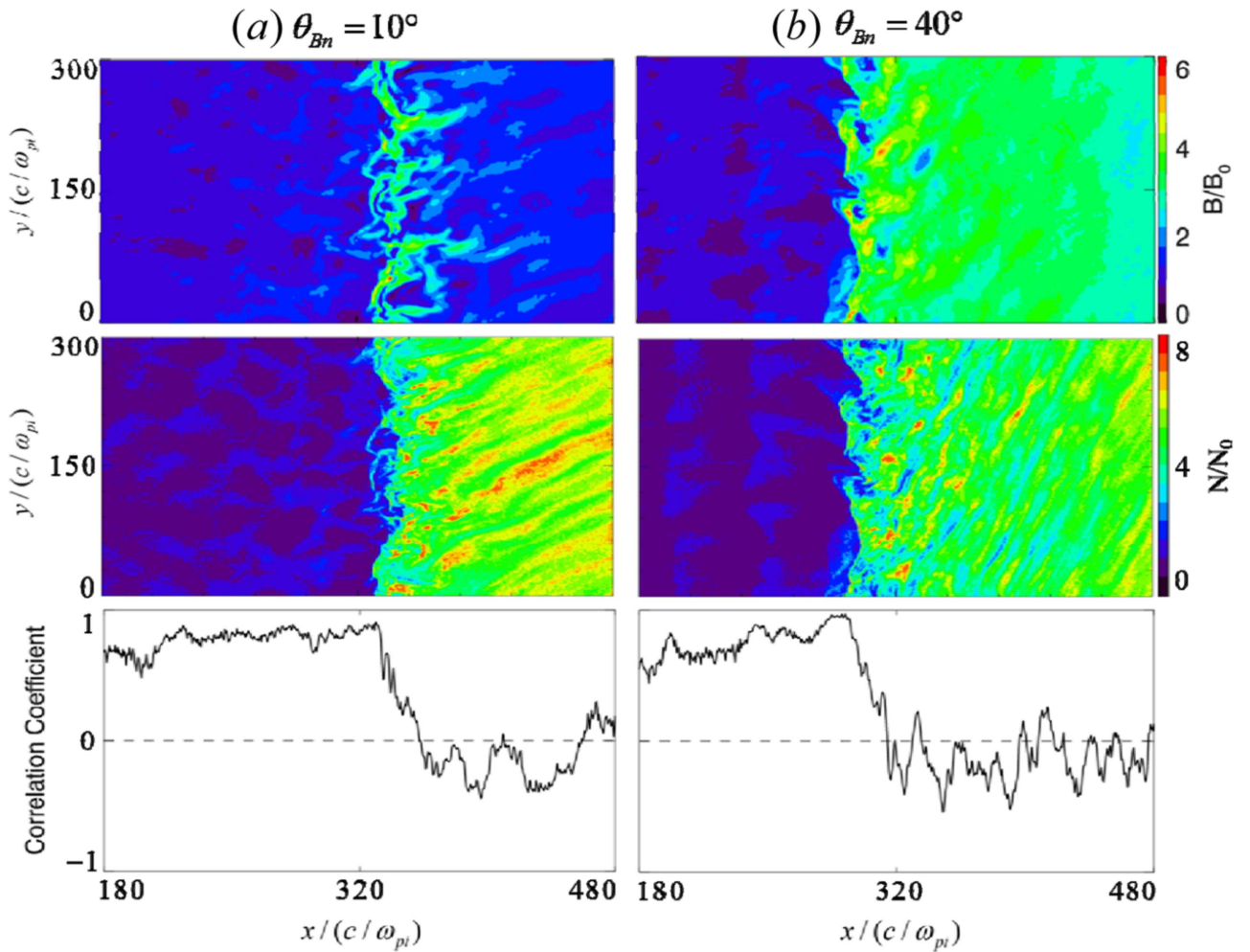


**Figure 8.** The contours of (top) the total magnetic fields, (middle) the particle number density, and (bottom) the correlation coefficient of the total magnetic field and particle number density at  $\Omega_i t = 161.5$  under different shock angle, (a)  $\theta_{Bn} = 10^\circ$  and (b)  $\theta_{Bn} = 40^\circ$ .

upstream electric fluctuations result from the mentioned upstream ULF waves. In the downstream region, electric structures for these two components are also filamentary as shown in Figure 2, and these structures have the potential to facilitate particle scattering across the shock front and make the Diffusive Shock Acceleration more efficient. Specifically, the corresponding wave spectra are very similar to those of fluctuations of number density, which implies that the KSWs are the dominant wave modes in downstream of the quasi-parallel shock under this condition.

To further investigate the role of KSW in the downstream of quasi-parallel shocks, we have also performed six runs under varying different shock conditions, including different shock angle  $\theta_{Bn}$ , Mach number, and plasma beta. The simulation results are displayed in the following three figures. In Figure 8, under a different shock angle, we display the total magnetic field, particle number density, and their correlation coefficient corresponding to  $\theta_{Bn} =$  (a)  $10^\circ$  and (b)  $40^\circ$  at time  $\Omega_i t = 161.5$ . In the upper panels, we can see the rippled shock fronts located, respectively, at  $x = 340c/\omega_{pi}$  and  $305c/\omega_{pi}$ , and the strongly fluctuated upstream and downstream similar to Figure 1. Also, the downstream particle number density from these two runs also shows filamentary structures, while they lie in different directions due to the different shock angle and the

resulting different directions of downstream background magnetic fields. However, unlike in Figure 3(a) and the run with  $\theta_{Bn} = 10^\circ$ , the correlation coefficient in the run with  $\theta_{Bn} = 40^\circ$  oscillates around zero, which implies that the amplitude of downstream KSWs is comparable to some transverse wave modes, which will weaken the relation between magnetic field and number density fluctuations. Additionally, they might be the mode converted Alfvén/ion cyclotron waves from upstream ULF waves in the shock front (Krauss-Varban & Omidi 1991).

In Figure 9, we show the results of two runs with different Mach numbers  $M_A =$  (a) 2.8 and (b) 6.8 in the same format as Figure 8. It seems that shock Mach number can strongly affect the downstream fluctuations of the magnetic field and particle number density as well as upstream ULF waves. As we can see in the upper and middle panels, the amplitudes of both the upstream and downstream fluctuations in the run with  $M_A = 2.8$  are lower than that of the run under  $M_A = 6.8$ , and their correlation coefficient indicates that for high Mach number shocks downstream, KSW may play a more dominant role compared to the proposed transverse Alfvén/ion cyclotron waves. Similarly, upstream plasma beta can also play an important role in the downstream dominant waves as is shown in Figure 10, where the simulation results are presented in the

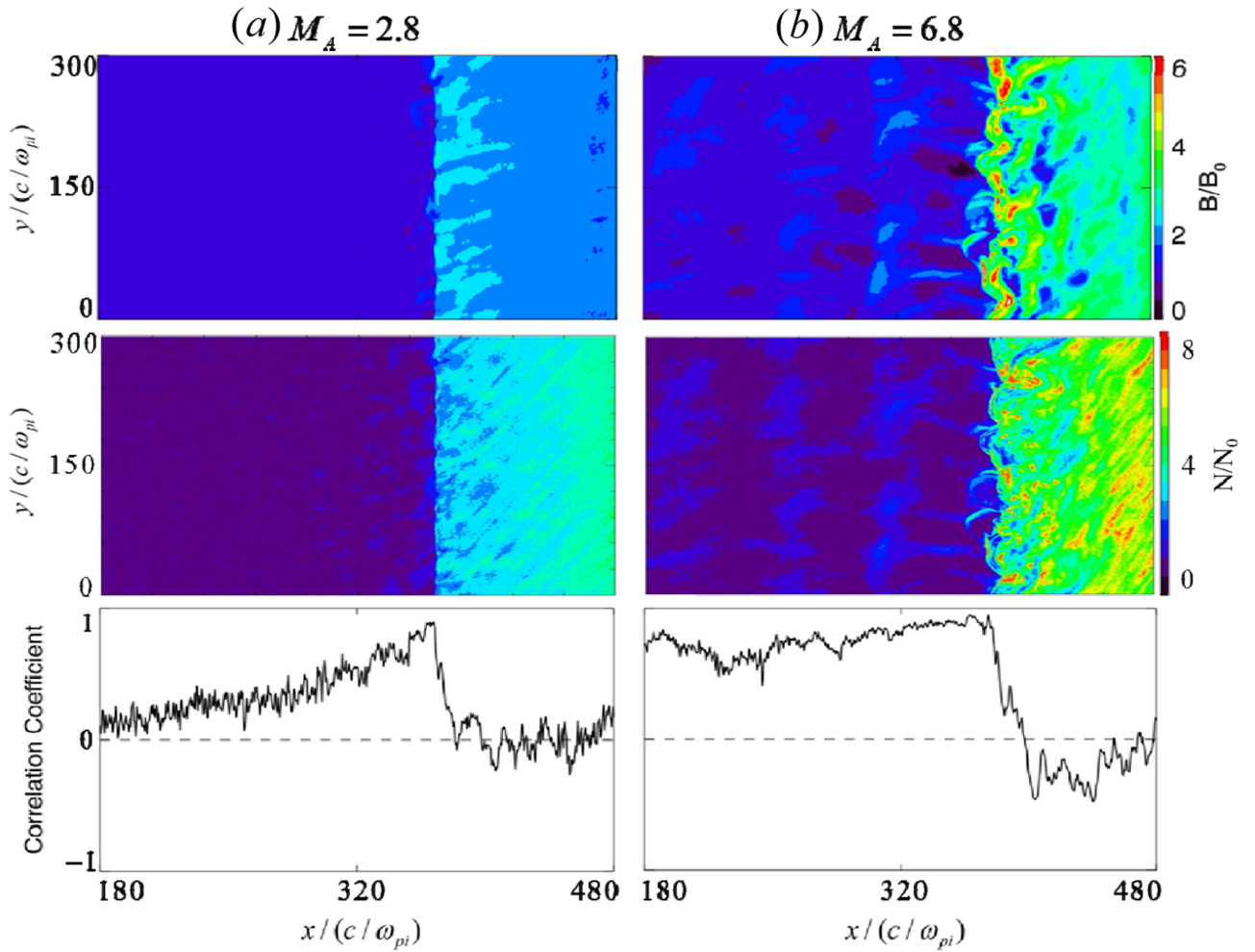


**Figure 9.** The contours of (top) the total magnetic fields, (middle) the particle number density, and (bottom) the correlation coefficient of the total magnetic field and particle number density under different Mach numbers, (a)  $M_A = 2.8$  and (b)  $M_A = 6.8$ .

same format under different upstream plasma beta values  $\beta_i =$  (a) 0.3 and (b) 1.0. The downstream number density fluctuations in both of the runs all show filamentary structures, and the correlation coefficient in the run with  $\beta_i = 1.0$  presents a strong anticorrelation between number density and total magnetic field in the downstream, while for the run with  $\beta_i = 0.3$ , their anticorrelation is weak so that the correlation coefficient varies around zero. Therefore, KSW has a dominant role in the downstream of quasi-parallel shock with higher upstream plasma beta.

#### 4. Conclusions and Discussion

In this paper, we identified the KSWs in the downstream of a supercritical quasi-parallel shock by comparing the magnetic field polarization ratio, Alfvén ratio, cross helicity, and compressibility with theoretical results. The magnetic field polarization ratio and Alfvén ratio are consistent with the properties of KSWs in the relations derived by Zhao et al. (2014). Additionally, the cross helicity and compressibility also reveal the existence of oblique slow waves and highly oblique KSWs (Gary & Winske 1992; Zhao et al. 2014). Therefore, we believe that KSWs exist in the downstream region of the quasi-parallel shock and that they are associated with the downstream filamentary structures of the number density of particles. Under

ceratin conditions, like smaller shock angle, higher Mach number, and upstream plasma beta, KSWs tend to become dominant downstream waves. Observations show a turbulent terrestrial magnetosheath (Alexandrova 2008; Alexandrova et al. 2008; He et al. 2011; Chaston et al. 2013) and indicate that compressive components are dominant over transverse fluctuations for more than half of the events of turbulence observed by cluster in the magnetosheath (Huang et al. 2017). Therefore, we consider that KSWs may be a candidate for the compressive components in the turbulent magnetosheath.

The slow mode was not noticed before because it can be strongly damped, so that it will hardly be found in a plasma (Chen & Wu 2011). Narita & Marsch (2015) demonstrated that quasi-perpendicular KSWs will be weakly damped and the damping rate will decrease when increasing the propagation angle. Hence, it is reasonable that they might form the observable compressive components of turbulence in the terrestrial magnetosheath behind the quasi-parallel shock and finally result in non-propagating pressure-balanced structures (PBSs) characterized by anti-correlations between the magnetic pressure and the thermal pressure (Yao et al. 2011, 2013; Howes et al. 2012; Yang et al. 2017). Even in solar wind, KSWs generated in the shocked plasma may be a possibility for the compressive component of the turbulence; although, in other astrophysical environments like the Very Local

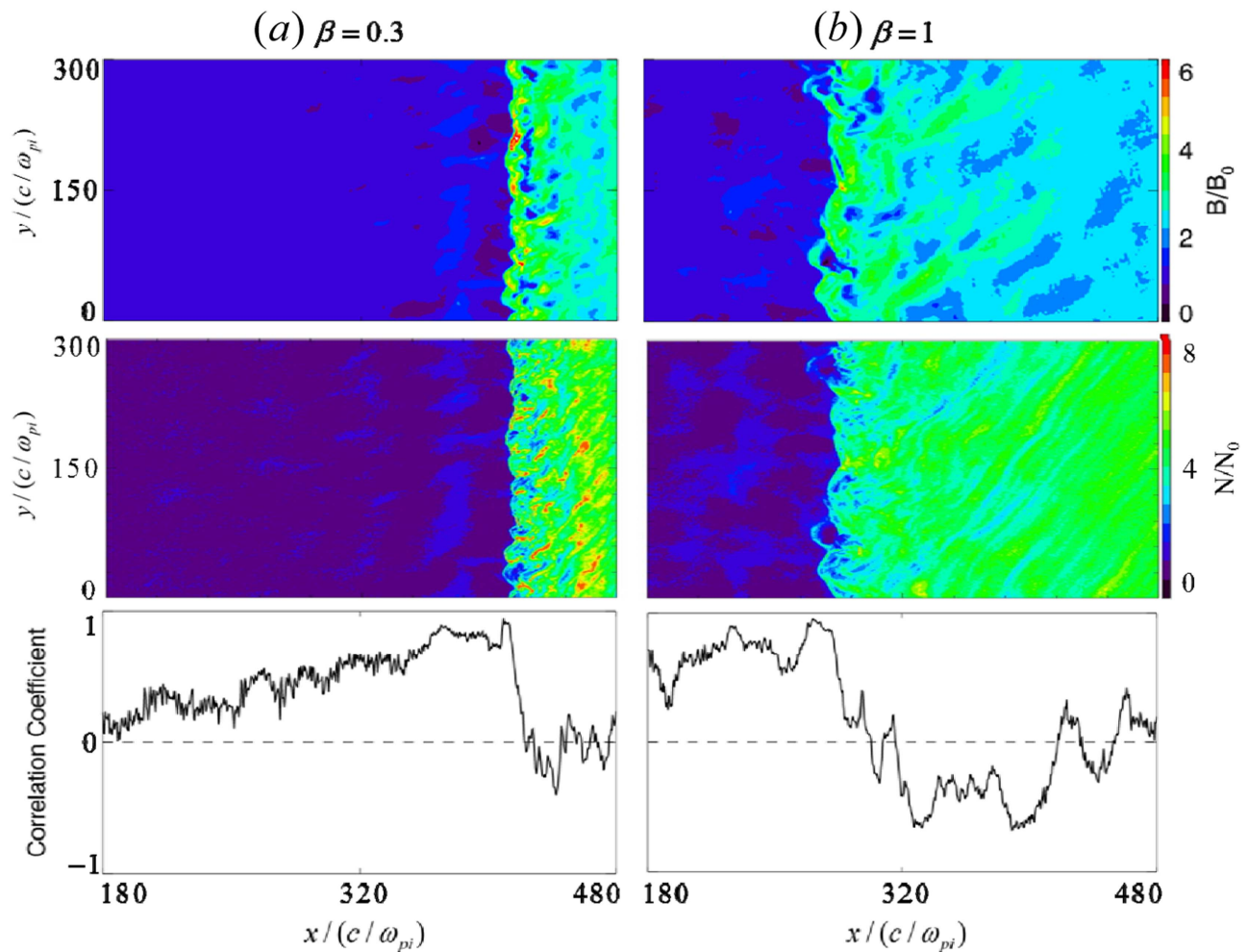


**Figure 10.** The contours of (top) the total magnetic fields, (middle) the particle number density, and (bottom) the correlation coefficient of the total magnetic field and particle number density under different plasma beta values, (a)  $\beta_i = 0.3$  and (b)  $\beta_i = 1.0$ .

Interstellar Medium, compressive fluctuations may originate from fast magnetosonic waves (Zank et al. 2017).

The work was supported by the NSFC grants 41331067, 41527804, 11235009, 41331070, 41421063, Key Research Program of Frontier Sciences, CAS(QYZDJ-SSW-DQC010), the Specialized Research Fund for State Key Laboratories, the Fundamental Research Funds for the Central Universities (WK2080000109) and Anhui Provincial Natural Science Foundation (1808085QD101). Y.H. was supported by the China Postdoctoral Science Foundation, grant No. 2016M602019. The simulation data will be preserved on a long-term storage system and will be made available upon request to the corresponding author.

#### ORCID iDs

Quanming Lu <https://orcid.org/0000-0003-3041-2682>

Xinliang Gao <https://orcid.org/0000-0003-0767-2267>

Dejin Wu <https://orcid.org/0000-0001-8058-2765>

#### References

- Alexandrova, O. 2008, *NPGeo*, **15**, 95  
 Alexandrova, O., Lacombe, C., & Mangeney, A. 2008, *AnGeo*, **26**, 3585  
 Chaston, C. C., Yao, Y., Lin, N., Salem, C., & Ueno, G. 2013, *JGRA*, **118**, 5579  
 Chen, L., & Wu, D. J. 2011, *PhPI*, **18**, 072110  
 Eastwood, J. P., Balogh, A., Dunlop, M. W., Horbury, T. S., & Dandouras, I. 2002, *GeoRL*, **29**, 2046  
 Eastwood, J. P., Balogh, A., Lucek, E. A., Mazelle, C., & Dandouras, I. 2005a, *JGR*, **110**, A11219  
 Eastwood, J. P., Balogh, A., Lucek, E. A., Mazelle, C., & Dandouras, I. 2005b, *JGR*, **110**, A11220  
 Eastwood, J. P., Balogh, A., Mazelle, C., Dandouras, I., & Reme, H. 2004, *GeoRL*, **31**, L04804  
 Gary, S. P. 1986, *JPh*, **35**, 431  
 Gary, S. P., & Winske, D. 1992, *JGR*, **97**, 3103  
 Giacalone, J., & Decker, R. B. 2010, *ApJ*, **710**, 91  
 Guo, F., & Giacalone, J. 2013, *ApJ*, **773**, 158  
 Hao, Y., Gao, X., Lu, Q., et al. 2017, *JGRA*, **122**, 6385  
 Hao, Y., Lembège, B., Lu, Q., & Guo, F. 2016a, *JGRA*, **121**, 2080  
 Hao, Y., Lu, Q., Gao, X., et al. 2014, *JGRA*, **119**, 3225  
 Hao, Y., Lu, Q., Gao, X., & Wang, S. 2016b, *ApJ*, **823**, 7  
 He, J. S., Marsch, E., Tu, C. Y., et al. 2011, *JGRA*, **116**, A06207  
 Howes, G. G., Bale, S. D., Klein, K. G., et al. 2012, *ApJL*, **753**, L19  
 Huang, S. Y., Hadid, L. Z., Sahrroui, F., Yuan, Z. G., & Deng, X. H. 2017, *ApJL*, **836**, L10  
 Jones, F. C., & Ellison, D. C. 1991, *SSRv*, **58**, 259  
 Krauss-Varban, D. 1995, *AdSpR*, **15**, 271  
 Krauss-Varban, D., & Omid, N. 1991, *JGR*, **96**, 17715  
 Narita, Y., & Marsch, E. 2015, *ApJ*, **805**, 24  
 Ofman, L., & Gedalin, M. 2013, *JGRA*, **118**, 1828  
 Omid, N., Berchem, J., Sibeck, D., & Zhang, H. 2016, *JGRA*, **121**, 3155  
 Omid, N., Sibeck, D., Gutynska, O., & Trattner, K. J. 2014, *JGRA*, **119**, 2593  
 Omid, N., Zhang, H., Sibeck, D., & Turner, D. 2013, *JGRA*, **118**, 173  
 Scholer, M., Fujimoto, M., & Kucharek, H. 1993, *JGR*, **98**, 18971  
 Scholer, M., Kucharek, H., & Jayanti, V. 1997, *JGR*, **102**, 9821  
 Shan, L., Lu, Q., Wu, M., et al. 2014, *JGRA*, **119**, 237

- Shan, L., Mazelle, C., Meziane, K., et al. 2016, [JGRA](#), **121**, 7385
- Su, Y., Lu, Q., Gao, X., Huang, C., & Wang, S. 2012a, [PhPI](#), **19**, 092108
- Su, Y., Lu, Q., Huang, C., et al. 2012b, [JGR](#), **117**, A08107
- Tsubouchi, K., Nagai, T., & Shinohara, I. 2016, [JGRA](#), **121**, 1233
- Wilson, L. B., III, Koval, A., Sibeck, D. G., et al. 2013, [JGRA](#), **118**, 957
- Yang, L. P., He, J., Tu, C., et al. 2017, [ApJ](#), **836**, 69
- Yang, Z. W., Lu, Q. M., Lembège, B., & Wang, S. 2009a, [JGR](#), **114**, A031111
- Yang, Z. W., Lu, Q. M., & Wang, S. 2009b, [PhPI](#), **16**, 124502
- Yao, S., He, J. S., Marsch, E., et al. 2011, [ApJ](#), **728**, 146
- Yao, S., He, J. S., Tu, C. Y., & Wang, L. H. 2013, [ApJ](#), **774**, 59
- Zank, G. P., Du, S., & Hunana, P. 2017, [ApJ](#), **842**, 114
- Zank, G. P., Rice, W. K. M., le Roux, J. A., Cairns, I. H., & Webb, G. M. 2001, [PhPI](#), **8**, 4560
- Zank, G. P., Rice, W. K. M., & Wu, C. C. 2000, [JGR](#), **105**, 25079
- Zhao, J. S., Voitenko, Y., Yu, M. Y., Lu, J. Y., & Wu, D. J. 2014, [ApJ](#), **793**, 107